Nanoscale

Accepted Manuscript

This article can be cited before page numbers have been issued, to do this please use: R. Bergamaschini, R. Plantenga, M. Albani, E. Scalise, Y. Ren, H. I. Hauge, S. Koelling, F. Montalenti, E. Bakkers, M. A. Verheijen and L. Miglio, *Nanoscale*, 2021, DOI: 10.1039/D0NR08051A.

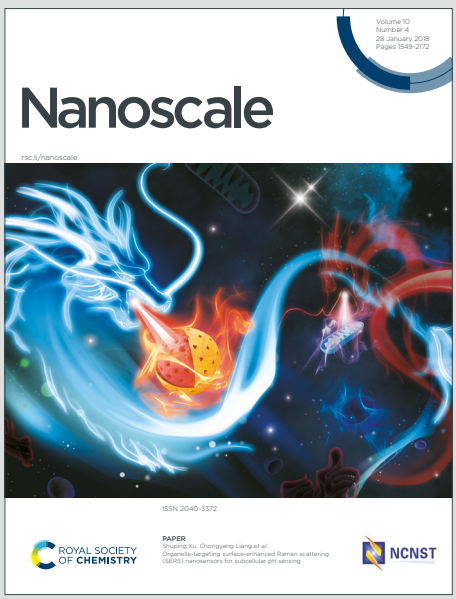

ROYAL SOCIETY OF CHEMISTRY

rsc.li/nanoscale

View Article Online
DOI: 10.1039/D0NR08051A

ARTICLE

Prismatic Ge-rich inclusions in the hexagonal SiGe shell of GaP-Si-SiGe nanowires by controlled faceting

Received 00th January 20xx,
Accepted 00th January 20xx

DOI: 10.1039/x0xx00000x

Roberto Bergamaschini,*[a] Rianne C. Plantenga,*[b] Marco Albani,[a] Emilio Scalise,[a] Yizhen Ren,[b] Håkon Ikaros T. Hauge,[b] Sebastian Kölling,[b†] Francesco Montalenti,[a] Erik P. A. M. Bakkers,[b] Marcel A. Verheijen,[b] and Leo Miglio [a]

The formation of Ge-rich prismatic inclusions in the hexagonal SiGe shell of GaP-Si-SiGe nanowires is reported and discussed in connection to a growth model that explains their origin. An accurate TEM/EDX analysis shows that such prisms develop right on top of any {11-20} facet present on the inner GaP-Si surface, with the base matching the whole facet extension, as large as tens of nanometers, and extending up to a thickness comparable in size within the SiGe shell. An enrichment in Ge by around 5% is recognized within such regions. A phase-field growth model, tackling both the morphological and compositional evolution of the SiGe shell during growth, is exploited to assess the mechanism behind the prism formation. A kinetic segregation process, stemming from the different surface mobility between Ge (faster) and Si (slower), is shown to take place, in combination with the evolution in the SiGe shell morphology. Actually, the latter moves from the one templated by the underlying GaP-Si core, including both {10-10} and {11-20} facets, to the more energetically convenient hexagon, bounded by {10-10} facets only. Simulations are shown to accurately reproduce the experimental observations for both regular and asymmetric nanowires. It is then discussed how a careful control of the GaP core faceting, as well as a proper modulation of the shell growth rate, allow for a direct control on the appearance and size of the Ge-rich prisms. This tunability paves the way for a possible exploitation of this lower-gap regions for advanced designs of band-gap-engineering.

Introduction

Nanowires (NW) are a clear manifestation of how far the growth kinetics may divert a system from its absolute thermodynamic minimum. The intrinsic low-dimensionality and axial symmetry return unique properties, totally different from the bulk or from a conventional planar film. NWs can be proficiently exploited as a platform for building integrated heterostructures,[1,2] both on-axis and radially, as in the widely exploited core-shell architecture. Complex multi-layered shells, obtained by alternating the deposition of different compounds, are commonly reported in the literature for fabricating concentric quantum-wells with carefully designed band-structures.[3,4] Potential applications space within optoelectronics,[1] photovoltaics,[5] lasers,[6] quantum computing,[7] … . Using a NW as "substrate" for heteroepitaxy may also be a convenient strategy to fabricate meta-stable materials, not accessible by standard growth. For example, in Ref. 8 GeSn shell layers, with Sn content exceeding by far the thermodynamic solubility of Sn in Ge, have been obtained on Ge core wires thanks to the enhanced strain relaxation offered by the axial morphology with respect to a planar one. Another key example is the recent achievement[9,10] of Si and Ge in their hexagonal phase (lonsdaleite), thanks to the templating effect of a wurtzite (GaP or GaAs) NW core.

When alloy materials are deposited as shells, segregation effects are frequently observed, resulting in a complex interplay between morphology and composition. A wide literature[4,11–15] shows that ternary III-V shells on core wires ubiquitously develop nanometre-thin spokes departing from the core edges and extending to the shell ones, eventually modulated by polarity effects.[16,17] A similar feature was also reported in Ge-GeSn core-shell NWs.[8,18] The formation of these non-uniformities has been attributed to a difference in mobility between the growth species giving one species an advantage over the other when diffusing away from the high-energy area of shell facet edges.[19] More complex patterns, with multiple radial lines, have been recently reported in GaAsP shells,[20] while in Ref. 3, the segregation stripes were found to open into three-dimensional quantum dots. Sunburst-like segregation has been also reported for quaternary alloys, as in the case of AlGaInAs/GaAs in Ref. 21 where it overlaps to broader segregation of In, possibly resenting of strain relaxation. Strain was also recognized as a driving force for the formation of nanodisks by Bi segregation in coaxial GaAs/GaAsBi/GaAs core–multishell NWs.[22]

[a] L-NESS and Department of Materials Science, University of Milano Bicocca, 20125 Milano, Italy.
[b] Department of Applied Physics, Eindhoven University of Technology, Groene Loper 19, 5612AP Eindhoven, The Netherlands.
† Present address: Department of Engineering Physics, École Polytechnique de Montréal, Montréal, Québec, Canada H3C 3A7
* Corresponding authors. E-mail: roberto.bergamaschini@unimib.it (theory); r.c.plantenga@tue.nl (experiments)
Electronic Supplementary Information (ESI) available: Details of the Phase-field model; DFT calculation of (11-20) and (10-10) GaP surface energy; Elastic strain calculations; VLS-GaP vs. VS-GaP growth morphologies; Additional data on EDX analysis; TEM structural characterization. See DOI: 10.1039/x0xx00000x

View Article Online DOI: 10.1039/D0NR08051A

Additional features emerge when different sets of facets compete on the growth front, i.e. when the core faceting differs from the one of the growing shell. Prism-like structures have been reported [11,12] for the overgrowth of a GaAs NW with an AlInP shell when facet rotation is observed during shell overgrowth. In-rich triangular prisms were also found in GaN-InGaN core-shell systems,[23] forming on top of {11-20}-nanofacets present in between the main {10-10} facets of the GaN core, similar to the GaN wires obtained at facet edges of GaN/AlN templates in Ref. 24. In Ref. 25, kinetic segregation into prism-like structures was also recognized in Ge-GeSn NWs in consequence of faceting transition, depending on the growth conditions. Coexistence of wires and dots at NW edges, resulting by on-axis twinning, has also been reported.[26] Facet-dependent incorporation dynamics was also found to be responsible of non-uniform composition profiles, even during the droplet-catalysed growth of Be-doped GaAs NWs.[27]

All of these local changes in composition may result in significant changes in material properties, altering the band structure and eventually returning quantum confinement effects.[3,28] These may be detrimental for the performances of any device conceived with the requirement of uniform composition but could also be exploited as active part of the heterostructure, opening new design possibilities. Controlling and tuning the self-assembly of such structures may add a degree of freedom for band-engineering, hardly achievable by top-down strategies.

In the present study, we focus on lonsdaleite SiGe shells, recently demonstrated[29,30] to grow with high crystal quality by using wurtzite GaP NWs with a Si-rich spacer shell templating for epitaxial SiGe shells. The in-depth structural analysis in Refs. 9 and 29 proved how the lonsdaelite phase can indeed be obtained uniformly along the GaP core NW, without any evidence of polytypism. Only partial defects have been observed.[31] The achievement of growing group IV shells in hexagonal phase, firstly demonstrated for pure Si,[9] is of great importance, as the band structure is different from the one of the cubic phase, resulting in a direct band gap in k-space at sufficiently high Ge content.[32,33] The band gap of this SiGe can be tuned by changing the Si:Ge ratio. This is a breakthrough for the achievement of efficient light emission and absorption[10] from group-IV integrated optoelectronic devices, curing the poor performances of the indirect gap, low emission efficiency cubic Si[34] without the need for III-V compounds.

However, here we show that this way of producing londsdaleite SiGe can lead to compositional inhomogeneities, depending on the GaP core faceting. In particular, here we show that Ge-rich prisms are formed on top of any {11-20} facet, whenever present in addition to the most common {10-10} facets[29] at the surface of the underlying wurtzite GaP-Si-rich spacer template. Due to the higher Ge content, such prisms have a lower band gap and correspondingly should trap carriers, which could be used for moving them away from surfaces or contaminated regions. At larger concentration differences, the Ge enriched areas could even behave as quantum wells, or wires.[3,35] Eventually, by carefully tuning the shell and prism composition under Ge-rich conditions, fascinating designs with different regions with direct and indirect band gap can be envisaged, opening new opportunities of band-gap engineering.

As the facets of the GaP-Si-rich spacer system guide the formation of the Ge enriched inclusions, we show their appearance in two cases: one with a GaP-Si-rich spacer presenting regular facet size, and one with an irregular GaP-Si-rich spacer morphology, with varying facet size. The alloy structure of the SiGe shells and the facets of the core-shell system were studied by producing cross-section lamella using a Focused Ion Beam (FIB) and analyzing them with Transmission Electron Microscopy (TEM).

To understand the formation of the Ge-rich prisms, we employ a modelling similar to the one used to understand spokes formation in III-V alloy shells.[19] We demonstrate that the formation of these prism-shaped inclusions can, indeed, be qualitatively understood from the interplay of mobility of the alloy species and of the different stability of {10-10} and {11-20} facets between the growing SiGe shell and the underlying GaP core. From this analysis, we learn how the formation of these prisms can be directed by controlling the faceting of the core-shell NW.

Experimental

The experimental procedure employed for the growth of the reported samples is described here, followed by details on the fabrication of cross-sectional lamella in the FIB and the TEM modes used to analyze the lamellas. Then, the phase-field model used for simulating the growth and segregation is reviewed. For the detailed analysis of crystal structure and defects we refer the reader to previous literature studies[9,29,31] on samples grown under equivalent conditions, and to the Electronic Supplementary Information for the analysis on the present samples.

Sample growth

NWs are grown using metalorganic vapor phase epitaxy (MOVPE) , under identical conditions of the GaP-SiGe core-shell structures of Refs. 9 and 29. Gallium phosphide stems are produced using the vapor-liquid-solid (VLS) method with gold catalyst arrays patterned by nano-imprint (NI) lithography on a GaP (111)B substrate. The GaP stems are grown from phosphine (PH_3) and trimethylgallium (TMGa) precursors at 600-615˚C, while providing HCl gas to prevent tapering (growth similar to Ref. 36).

After this the sample is cooled down, the susceptor is changed and the sample is heated up to 570˚C again. A gallium phosphide shell is grown by vapor-solid (VS) deposition for 30s to 4min/240s, resulting in a wurtzite GaP-GaP core-shell template, after which the trimethylgallium flow is stopped. This additional GaP shell is required to retain an atomically flat, oxide-free template for the subsequent epitaxial SiGe growth. The sample temperature is increased to the growth temperature for the Si rich spacer, while the phosphine flow is continued creating an overpressure to prevent decomposition

of the GaP NWs. This spacer can either be a Si shell, or a SiGe shell rich in Si (around 86%). Disilane is used as silicon precursor, germane as germanium precursor. The final SiGe shell is grown by going to the SiGe growth temperature under hydrogen flow, without intermediate cooling down to room temperature. In case of the SiGe shell on a Si spacer the disilane flow is stopped, the cooling is done under hydrogen flow and disilane and germane flows are opened when reaching the set temperature (see Ref. 29). In case of the transition from a SiGe spacer to a SiGe shell the precursor flows are gradually adapted (also see Ref. 30).

Two sets of samples are studied, obtained from different growth conditions. The first set was grown targeting low-Ge content to minimize the role of strain. A nano-imprint pattern with a pitch of 500 nm was used. The GaP shell was grown for 4 min and the SiGe shell was grown at 575˚C. The group IV molar fraction of Ge in the input was 50%, resulting in a Ge concentration in the shell of around 30%. Then, to test the robustness of the results against higher strain levels, the second set of samples was grown with the main purpose of reaching higher Ge content in the shell. More precisely, the pitch was increased to 2500nm, a SiNx mask was introduced, the gold was etched before growing the spacer layer, the GaP shell growth was reduced to 0.5 min and the SiGe shell growth was performed at 495˚C. The group IV molar fraction of Ge in the input was 81%, resulting in a Ge concentration in the shell of around 45%.

Cross-sectional TEM

To study the NWs in cross-sectional view, lamellas were prepared using a focused ion beam (FIB). Several NWs are transferred and positioned parallel on a Si substrate. A protecting platinum strip is deposited across, on the region of interest. Sometimes an additional cobalt layer is deposited before the platinum to add a layer with more contrast in TEM. A volume is made, cutting the NWs across, and lifted out with a nanomanipulator. Subsequently the volume is transferred to a TEM substrate and thinned down using FIB milling to a thickness of around 100 nm or less.

The lamellas are studied in TEM, using mainly two modes: High angular annular dark field (HAADF) scanning TEM (STEM) imaging and energy dispersive (X-ray) spectroscopy (EDX). For HAADF imaging, the electrons scattered over large angles are used for imaging, to minimize the contribution of diffraction contrast to the image. The intensity of the signal is roughly proportional to the elemental number Z^2.[37] Therefore, HAADF imaging is very suitable to scan for compositional differences (like the ones we anticipate in the SiGe alloy shells). EDX is used to give a quantitative measure for the amount present of a certain element.

Phase-field model of growth and segregation

The phase-field growth model introduced in Ref. 38 and already applied to study segregation in core-shell NWs in Refs. 19,25 is adapted to the case of the SiGe shell growth. Under the assumption that the NW is uniform along its axis, a (0001), a two-dimensional (2D) cross-section is considered, as sketched in Fig. 1(a). The NW geometry is defined implicitly by the phase-field function φ (panel (b)), set equal to 1 into the solid phase and 0 in the surrounding vacuum region. A smooth transition region of thickness $\epsilon \to 0$ is assumed in-between, thus returning a diffuse-interface.[39] Nominally, the NW surface is identified with the φ=0.5 iso-line. A second variable, c, is used to locally define the Ge content in the NW shell (panel (c)). For numerical reasons, c is defined over the whole simulation cell including vacuum and core regions where it has no physical significance. Both faceting evolution and compositional segregation effects are taken into account by solving simultaneously the temporal evolution of both φ and c, as given by the following equations:

$$\frac{\partial \varphi}{\partial t} = \mathrm{R}|\nabla\varphi| + \nabla \cdot [cM_{\mathrm{Ge}}M(\varphi)\nabla\mu_{\mathrm{Ge}}] + \\ + \nabla \cdot [(1-c)M_{\mathrm{Si}}M(\varphi)\nabla\mu_{\mathrm{Si}}] \quad (1)$$

$$\frac{\partial (c\varphi)}{\partial t} = \mathrm{R}_{\mathrm{Ge}}|\nabla\varphi| + \nabla \cdot [cM_{\mathrm{Ge}}M(\varphi)\nabla\mu_{\mathrm{Ge}}] \quad (2)$$

where $\mathrm{R} = \mathrm{R}_{\mathrm{Ge}} + \mathrm{R}_{\mathrm{Si}}$ is the total deposition rate, i.e. the sum of Si and Ge growth rates. M_{Ge} (M_{Si}) is the mobility of Ge (Si) atoms on the NW surface. In the present study a mobility ratio $M_{\mathrm{Ge}}/M_{\mathrm{Si}}$=10 is assumed.[40,41] The function $M(\varphi) = (36/\epsilon)\varphi^2(1-\varphi)^2$ is introduced for restricting the motion only within the phase-field interface,[42] so to enforce surface diffusion dynamics (bulk diffusion is negligible as implied by higher

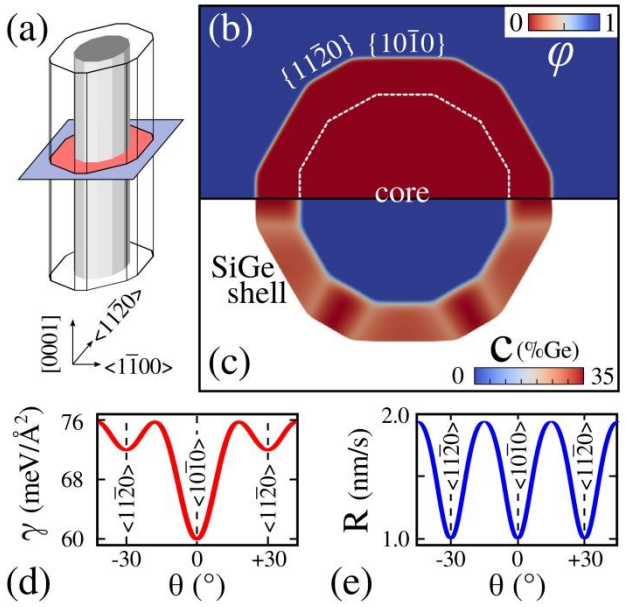

Fig. 1 (a) Modeling of the (0001), 2D cross-section of the NW. Both (b) the phase-field function φ and (d) the composition field c are illustrated by the color map for a representative case. In (c) the NW section is taken as the region for $\varphi \geq 0.5$. The NW core, delimited by the white dotted line in panel (b), is set to be a pure-Si region for simplicity and it is used as initial profile in the growth simulations. Plots of (d) surface energy density γ and (e) growth rate R as a function of the profile orientation θ.

activation barriers). Intermixing is then possible only within the $\sim \epsilon$-thick interfacial region, i.e. within the first atomic layers of the NW surface.[41,43]

μ_{Ge} (μ_{Si}) is the surface chemical potential for Ge (Si) and its gradient is the driving force for Ge (Si) surface diffusion. Here we assume that μ comprises only anisotropic surface energy, corner energy,[44] and mixing entropy (for an ideal alloy):[43]

$$\mu_i = \kappa[\gamma + \gamma''(\theta)] - \beta\left(\frac{d^2\kappa}{ds^2} + \frac{\kappa^3}{2}\right) + \frac{kT}{V_a}\ln c_i \qquad (3)$$

where V_a is the volume per atom, κ is the surface curvature, γ is the surface energy density, dependent on the profile orientation θ, β is a corner-energy parameter, k is the Boltzmann constant and T the temperature. In strong anisotropy conditions, the corner contribution is necessary for regularization.[44] The actual phase-field expression of eq. (3), as a function of φ, is widely discussed in literature,[19,42,45] and it is reported in the Electronic Supplementary Information.

It is worth noting that the definition of μ_i in eq. (3) is purposely including only those key contributions leading to the morphological and compositional evolution found experimentally. The major approximation of this minimalistic model is the exclusion of strain effects due to the SiGe/Si lattice mismatch. This simplification is, however, quite reasonable when considering a low-Ge shell alloy, 30% in the present simulations, as strain relaxation is expected to be quite effective for the NW geometry. A thorough calculation of the strain distribution in the shell, as detailed in the Electronic Supplementary Information, shows that strain is released equally effective on the {10-10} and {11-20} facets that will be shown to be essential for the prism segregation. Moreover, the experiments show a rather similar behavior when raising the Ge concentration from 30% to 45%, thus corroborating the hypothesis that elasticity is not the main driving force for the prism formation in our system. A further confirmation of this hypothesis can also be found by noticing that segregation effects, similar to the ones here discussed, have been reported for III-V lattice-matched core-shell NWs.[11]

In order to describe the faceting of the SiGe shell, both γ and R are assumed as orientation dependent, with local minima for the six {10-10} and six {11-20} facets in the (0001) plane, as shown in panels (d) and (e) of Fig. 1, respectively. The convenient function of Ref. 45 is exploited. We consider {10-10} facets to be more stable than {11-20} ones, i.e. $\gamma_{10\bar{1}0} < \gamma_{11\bar{2}0}$, as confirmed by recent ab-initio calculations for pure Si and Ge lonsdaleite.[46] The actual simulation parameters are $\gamma_{10\bar{1}0}$=60 meV/Å^2 and $\gamma_{11\bar{2}0}$=72 meV/Å^2, reasonably scaled for a 30% Ge alloy but for a larger difference than the one obtained by a linear interpolation of the ab-initio values, so that the Wulff shape is a {10-10}-only hexagon as in experiments (see Electronic Supplementary Material). The growth rate is supposed instead to be the same for the two facets $\mathrm{R}_{10\bar{1}0} = \mathrm{R}_{11\bar{2}0} \approx 1$ nm/s (but slower than at corners, as expected for the kinetic Wulff construction[19]). An interface width ϵ=2 nm was set. Other parameters tuned to match experiments are β =150eV and kT/V_a=1.6 eV/nm^3.

Numerical solution to the partial differential equations (1-3) is obtained by the finite element method toolbox AMDiS.[47,48] Local mesh refinement (with a maximum resolution of 2Å) and a semi-implicit time-integration scheme are exploited.

Results and discussion

Experimental observation of Ge-rich prisms

To investigate the compositional structure of the core-shell NWs lamellas were studied with HAADF-STEM, since HAADF contrast is mainly depending on the average atomic weight. The HAADF images of a (0001) cross-section sample with 42% Ge in the SiGe shell reported in Fig. 2(a) and (b) show the characteristic core-shell NW build-up. At the center there is a wurtzite GaP core surrounded by a Si-rich spacer shell (dark contrast) and the lonsdaleite SiGe shell. On the outer side of the SiGe shell a Ge-rich layer is visible (light contrast). This layer forms during cool down, which is mainly attributed to the fact that the Ge precursor needs a lower temperature than the Si precursor to crack efficiently, and therefore keeps on adding to the growth front for longer. The HAADF contrast between the different layers shows a clear transition in morphology between the GaP-Si inner region and the SiGe (and Ge) shell. As made evident by the atomic scale HR-STEM in Fig. 2(c), the former consists of both {10-10} and {11-20} facets, which are both non-polar singular facets in the hexagonal system. Differently, the outer shell shows a hexagonal shape, consisting of {10-10} facets only.

In the SiGe shell various inhomogeneities are observed. Segregation stripes can be identified running from the corners of the Si-rich spacer shell to the outer corner of the SiGe shell. Unlike in the case of III-V NWs, here the stripes are less prominent, and involve variations in composition of the order of 1%. Moreover, the HAADF contrast suggests a composite structure formed by an inner Ge-rich line in between Si-rich ones, probably due to secondary effects superimposed to the mechanism of accumulation of the slowest diffusing species at facet edges, well evident in III-Vs.[19]

More interestingly, Ge-rich triangular areas, which correspond to the prisms in three-dimensions, can be well distinguished (Fig. 2(b)) on half of the facets of the Si-rich spacer layer. From an EDX mapping (see Fig. 2(d-f)), the Ge concentration in the prisms was determined to be 50±3% compared to 42±2% in the shell in the areas without spokes. Neither Ga nor P are observed within the SiGe shell.[49] HR-STEM reveals that the facets the prisms are located on are the {11-20} facets. Since the SiGe shell develops a surface terminated by {10-10} facets only, and noting that the base of the prisms closely matches the size of the {11-20} facets, it is clear that the formation of the prisms is directly related to the {11-20} facets of the GaP-Si-rich structure.

View Article Online
DOI: 10.1039/D0NR08051A

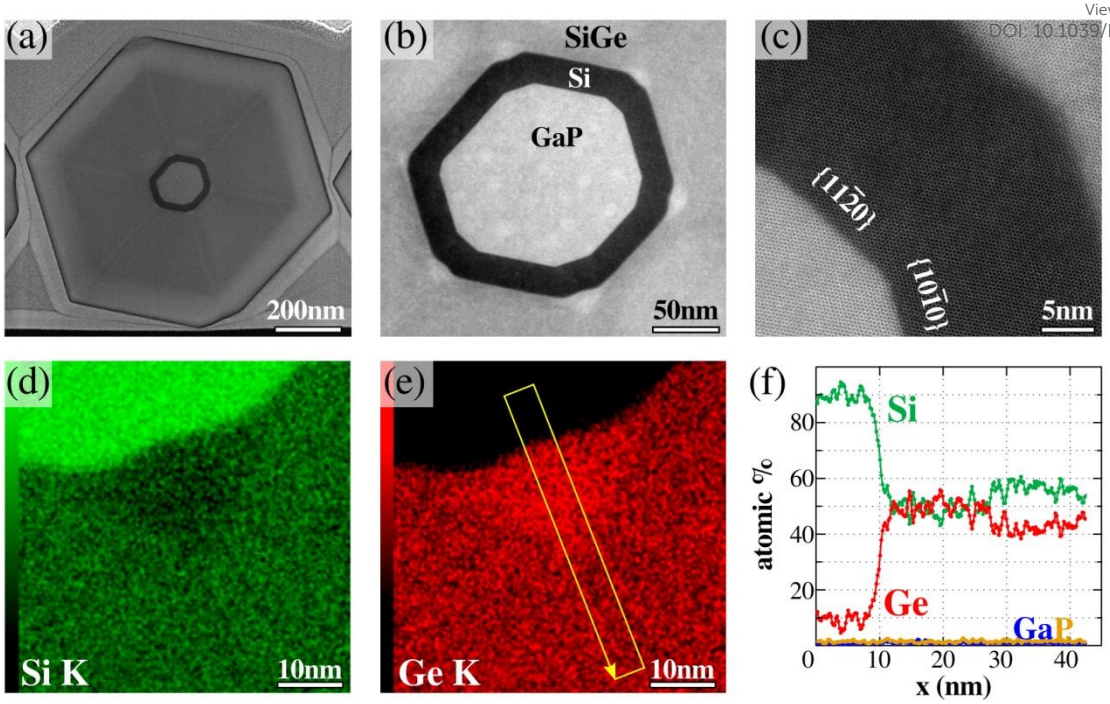

Fig. 2 (a) Cross-sectional view in HAADF-STEM of a wire with nominal composition of ~45% Ge in the SiGe shell. (b) Zoom-in on the central part of the wire shown in (a). (c) atomic resolution STEM image on part of the interfaces of (b). The crystal planes are indicated. (d,e) quantified elemental distribution maps of Si and Ge by EDX. (f) compositional profile extracted from the mappings in (d,e) averaged over the width of the box in (e). Ga and P lines are below the EDX detection level.

This connection is made even more evident in the HAADF-STEM image in Fig. 3(a), where the cross-section of a wire obtained for a different sample with nominal Ge content of ~30% in the shell is reported. Therein, an asymmetry in the GaP core shape is obtained, resulting in different widths of the {11-20} facets for the Si-rich spacer. Prisms in the SiGe shell are observed to match the different {11-20} base lengths (see Fig. 3(b)), extending across a larger shell thickness when developing on the largest facet, while being barely distinguishable at corners where {11-20} facets are almost missing. The EDX mapping, shown in panels (c) and (d), return a more direct view of the segregation process, demonstrating that prisms are enriched in Ge (33±3% with respect to the average shell Ge content of 26±3%) for all sizes. Expectedly, Ga and P are not detected in the SiGe shell, thus excluding their role in the segregation of the Ge-rich prisms. Interestingly, spiky protrusions of the two elements are instead noticeable across the Si spacer, only in correspondence of large {11-20} facets (see Electronic Supplementary Information). Si-rich stripes are found to depart from the apex of each prism to the outer shell corners. As the Si surface mobility is expected to be lower than the mobility of Ge,[40,41] this seems consistent with the diffusion induced segregation in III-Vs.[19] The apparent contrast with the case of Fig. 2 suggests, however, a more complex scenario especially in the case with higher Ge content. The fact that prisms are formed in both the low-strain and high-strain sample permits to exclude elasticity as a key driving force. Moreover, while in the case of Fig. 2 one could suspect that larger Ge atoms could be moving towards the

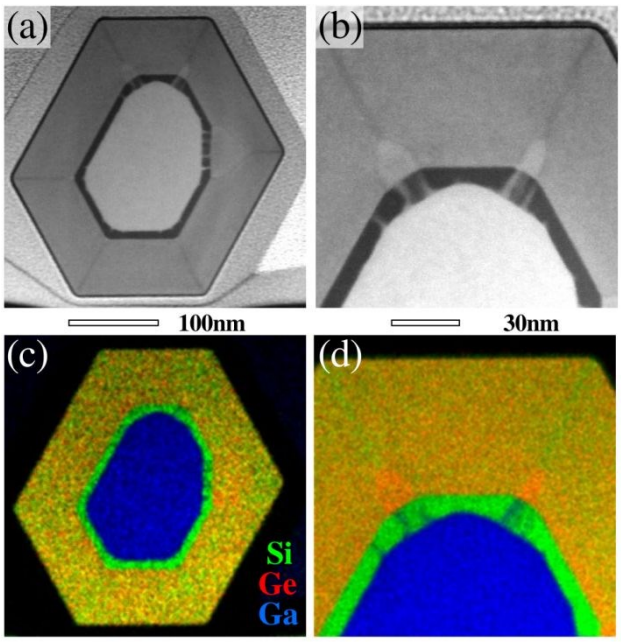

Fig. 3 (a) Cross-sectional view in HAADF-STEM of a wire with nominal composition of ~30% Ge in the SiGe shell. (b) Zoom-in showing a portion of the wire with differently sized prisms. (c) EDX analysis of the whole NW cross-section and (d) of the portion of panel (b). See Electronic Supplementary Information for the further details.

small {11-20} corners, where strain is better released (see Electronic Supplementary Information), in Fig. 3 we see the very same segregation process on much wider {11-20} facets, where no relaxation advantage is to be expected.

The cross-sectional TEM analyses of other NWs for both samples further confirmed the previous observation, showing Ge-rich prisms on top of any {11-20} facet present at the GaP-Si rich interface. Moreover, Ge-rich prisms have been also observed in samples where pitch, substrate surface, Si:Ge ratios, temperature and material influx were changed, as long as the {11-20} facets were present.

Simulation of the SiGe shell growth

The experimental STEM-EDX analysis provides clear evidence of the correlation between the formation of Ge-rich prisms in the SiGe shell and the presence of {11-20} facets at the underlying GaP-Si-rich spacer surface. By exploiting the PF growth model outlined in the method section, we now investigate the kinetic mechanism responsible of this segregation process.

The model relies on two major properties of SiGe. The first is that {10-10} facets are more stable than {11-20} ones, which is inferred from the experimental evidence that the SiGe shell cross-section evolves into a {10-10} hexagon in the present high-temperature and low-rate growth regime that is expected to be close to equilibrium. This definition is also consistent with recent data by first-principle calculations,[46] even if here a larger difference is required to achieve the facet transition. Due to this energetic unbalance, material will diffuse on top of the {11-20} facets, reducing their sizes in favor of the more energetically favorable {10-10} ones. The second key property is that Ge shows a greater mobility, as compared to Si, which is well known fact at the surfaces of the cubic system, [47-49] and is likely to hold true in the present case, as it is essentially related to atomic bond strength. Hence, any diffusion flux will be mostly composed of Ge. Regarding deposition, we just consider the same incorporation rate on the two facets and an enhanced rate at their corners, so to drive a conformal faceted growth without any local rounding at the corners as detailed in Ref. 19. Growth simulations are then performed starting from an initial dodecagonal profile, with both {10-10} and {11-20} facets, mimicking the GaP-Si core shape. We do not consider the internal core-spacer structure since mixing involves only the topmost atomic layers of the Si spacer. The evolution in the NW shell morphology and composition results from the competition between deposition and diffusion. The simulation results, reported in Fig. 4 for both a regularly shaped core (a-c) and an asymmetric one (d), closely resemble the experimental observations in Fig. 2 and 3. In particular, the appearance of Ge-rich regions on top of the {11-20} core facets is clearly revealed by the color map, and traced more quantitatively by the line plots across the shell thickness (Fig 4(b)), passing through the prism itself (segment A in panel (c)). In particular, prisms have ~ 34% Ge content, compared to the nominal 30% of the shell, in agreement to the experimental data shown in Fig 3. Si-rich spokes are also observed at the facet corners, departing from the prism apex out to the shell corners.

The growth process can be divided in two stages. In the first, both {10-10} and {11-20} facets are present as originating from the underlying GaP-Si spacer surface but, as the deposition continues, the latter shrink in size and finally disappear,

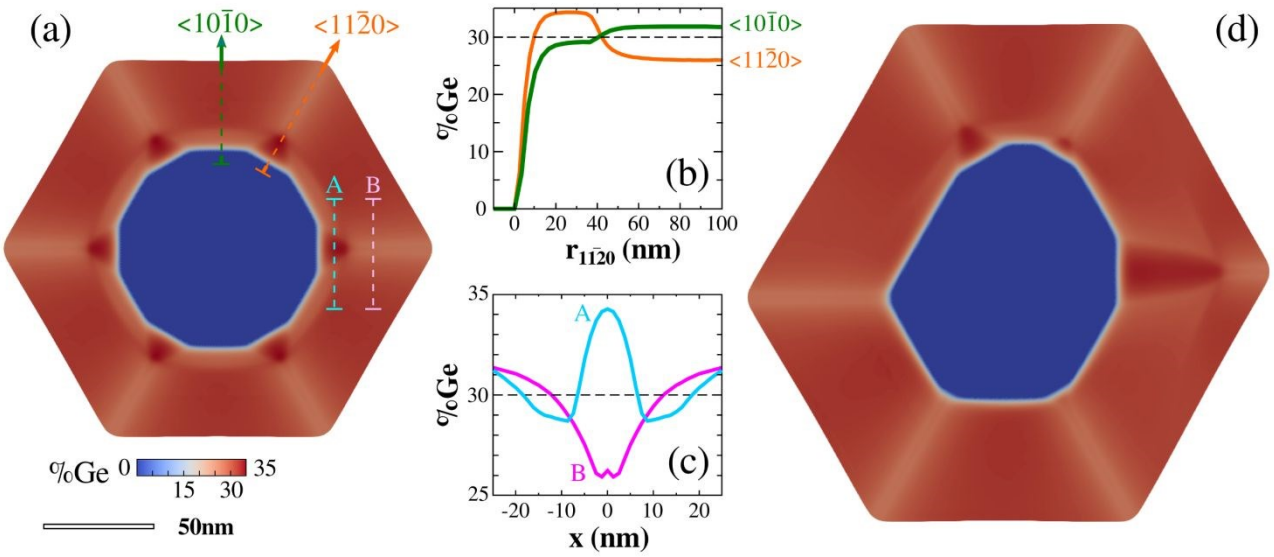

Fig. 4 Simulation results for a 30% SiGe shell growth on top of a (GaP-)Si core exposing both {10-10} and {11-20} facets. (a) A regular dodecagonal core of 90 nm diameter is considered and the composition profiles are traced (b) along the NW <10-10> and <11-20> radii, as a function of the shell thickness r_{11-20} along the latter direction, and (c) along segments trhough the prism (A) and through the spokes (B). (d) Evolution starting from an irregular core morphology with different facet extensions, mimicking the experimental one in Fig. 3.

resulting into the hexagonal cross-section. The origin for this faceting transition is the difference in surface energy, causing the diffusion of material, richer in Ge because of its higher mobility, on top of the {11-20} facets. Meanwhile, the shell thickness increases because of deposition, so that the segregation area extends into the prisms. Notably, the Ge content at the {10-10} facets is lowered by this transfer, even if this variation is smaller (~2%) as it spreads over the larger area of {10-10} facets, so that it is barely distinguishable by EDX measurements.

In the second stage of the shell growth, right after the {11-20} closure, narrow corner regions are left in between the {10-10} facets. As corners correspond to high energy sites, material tends to diffuse away from them. Due to the mobility difference, Si is left behind, forming the Si-rich spokes (see line B in Fig. 4(c)) and extending across the shell thickness, in the same way as commonly observed for III-V core-shell NWs.[19]

It is worth noting that both segregations in the two stages are a consequence of the directionality in the surface diffusion process, but with different origin. Prism segregation is due to a flat facet property, i.e. its surface energy, and hence it involves the whole facet extension. Si spokes are, instead, formed because of the larger surface energy at the high-curvature edges, point-like in cross section, so that their width is invariant and limited to a few nm as the shell grows larger.

The mechanism discussed here offers a direct explanation of the different size of the prisms in the case of asymmetric core shape of Fig. 3a and 4d. Indeed, the larger the original size of the {11-20} facet at the GaP-Si core surface, the longer is the time required to close it, i.e. the shell thickness at which it happens, thus resulting in a bigger prism. Vice versa, if the {11-20} facet is small, diffusion will cover its area rather immediately so that no prism is formed at the corner.

Assigning the facet formation on the GaP-Si spacer system and of the SiGe shell to energetic terms makes the driving mechanism for closing the facets distinctly different from the facet rotation described in zincblende AlInP by Sköld et al.[11], also analyzed for GaAs by Nötzel et al.[50]. Nötzel et al. explain the rotation in GaAs morphology by the fact that the {112} facet is a nonsingular facet formed under kinetic conditions, that breaks up in the singular facets, like {110}, when the energy barrier is overcome. This does not apply for the {10-10} and {11-20} hexagonal facets that are both singular facets. A greater similarity can be instead recognized with the case of Ref. 23 where In-rich prisms are found to form in InGaN shells right on top of {11-20} nano-facets present on the GaN core wires, but disappearing from the outer perimeter of the shell. There, strain effects and facet dependent nucleation dynamics, as discussed in Ref. 24 for the rather similar case of the formation of GaN wires on GaN-AlN NWs, are expected to have a role in the segregation process. However, despite the different driving force, the segregation mechanism leading to the prisms is rather similar and expectedly reproducible by slight changes in the modeling.

Predictions for the tunability of the Ge-rich prisms

View Article Online
DOI: 10.1039/D0NR08051A

Our analysis demonstrates by experiment and simulation that the origin of Ge-rich prisms comes from the existence of {11-20} facets at the early growth stages, which are energetically unfavorable for SiGe, and hence drive significant material flows to cover them. The one-to-one correspondence between the prism dimensions and the extension of such {11-20} facets on the GaP-Si core surface, evident in the case of asymmetric core, indicates the possibility to tune the prism size by controlling the faceting of the Si-rich spacer.

The origin of the {11-20} facets on the Si-rich spacer can be found by retracing the evolution of the {11-20} facets during the growth steps. GaP wurtzite NWs grown by VLS are mostly terminated by {10-10} facets.[36] However, the cross-sections of Fig. 2 and 3 already show {11-20} facets on the GaP templating for the Si-rich spacer. This means the {11-20} facets form during the VS GaP shell growth. Notably, even after growing a GaP shell for 45 min, a mix of {10-10} and {11-20} facets prevails (see Electronic Supplementary Information). Such considerations suggest that the appearance of both facets at the GaP shell in Fig. 2 and 3, after 0.5 and 4 min growth time respectively, should not be an intermediate growth stage, but rather a (meta)stable state.

In order to understand this phenomenon, we computed ab-initio the surface energy of both {10-10} and {11-20} for GaP, as detailed in the Electronic Supplementary Information. The

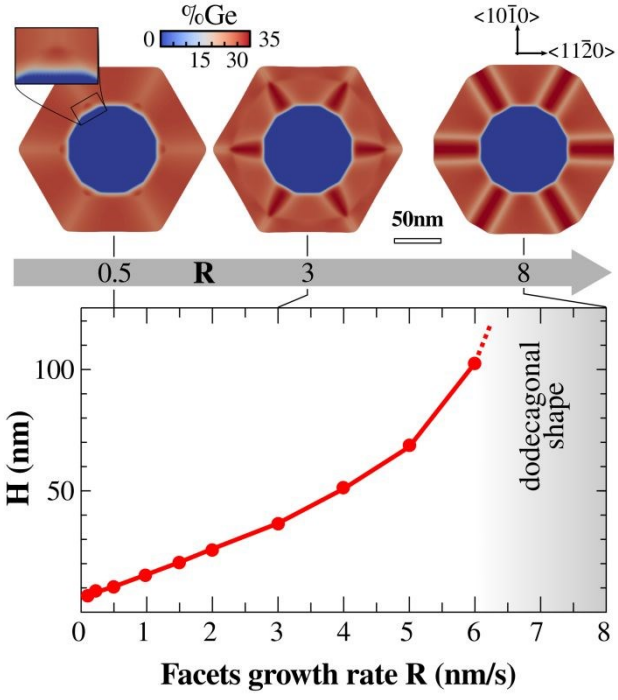

Fig. 5 Comparison of the shell morphological and compositional evolution at different growth rates R, starting from the same regular dodecagonal core of radius 90nm of Fig. 4(a). The extent of the segregation region increases with the growth rate as made evident by the plot of the prism height (H) as function of it.

View Article Online
DOI: 10.1039/D0NR08051A

obtained results, $\gamma_{10\bar{1}0}$=39.94 meV/Å^2 and $\gamma_{11\bar{2}0}$=40.90 meV/Å^2, are so close that, from an energetic point of view, both sets of facets are to be present in the equilibrium Wulff shape, that should be a nearly regular dodecagon. The absence of the {11-20} facet on the WZ GaP stem can easily be due to the fact that the stem is grown using a gold catalyst particle. The catalyzed growth brings differences in kinetics and energies. Viceversa, when considering the VS growth we expect a regime more influenced by thermodynamics, thus restoring the, equally stable {11-20} facets, to approach the Wulff shape. However, as proceeding from the out-of-equilibrium VLS hexagonal profile, a prominence of {10-10} facets is to be expected.

Since the VLS stem is terminated by {10-10} facets this transition opens up possibilities to tune which facets are present by tuning the amount of GaP overgrowth. Although some GaP deposition is needed to commence Si overgrowth, this can be limited to a short pulse to maintain the {10-10} faceting. On the other hand, longer VS overgrowth times will reveal {11-20} faceting. Similarly, a variation in the Si-spacer layer thickness could also be exploited to tune the sizes of {11-20} facets, prior to depositing the actual SiGe shell.

Another way to tune the prisms dimensions can be exploited by tuning of the flux vs. mobility ratio. Indeed, this permits to control the rate at which the thickness of the deposited shell increases with respect to the faceting transition time scale. This is illustrated in Fig. 5, where growth simulations were performed for the same core geometry, i.e. same initial size of {11-20} facets, and different deposition rate. In the case of slow deposition the material redistribution is dominant so that the faceting transition completes in a short time and the prisms are not distinguishable at all. Viceversa, as the deposition rate increases, the shell thickness at which the {11-20} facets close increases and correspondingly the prism height H increases. For large deposition rates, material transfer can be frustrated to the point they become insufficient to shrink the {11-20} facets, so that the initial dodecagonal shape is preserved also in the shell. Nonetheless, an enhancement of the Ge content at the {11-20} facets is still recognizable as trace of the, still active, diffusion process. The variation in the prism height H as a function of the growth rate is shown in the plot of Fig. 5, ranging from the limiting case of vanishingly small prism to the case of dodecagonal shell. According to the previous analysis, the reported trend is expected to depend on the extent of the initial {11-20} facets, so that both core geometry and growth conditions can be used for tuning the prisms dimensions.

Conclusions

Ge-rich prisms are reported to systematically form within shells of SiGe in hexagonal phase, on top of the {11-20} facets present at GaP-Si-rich core NWs. The modelling of the experimental findings shows that they are produced by a kinetic segregation during the faceting transition, from one “dodecagonal” morphology, with both {10-10} and {11-20} facets at the GaP-Si-rich spacer surface, to an hexagon morphology with {10-10} facets only, for the outer SiGe shell. The shape conversion, indeed, occurs during the first stages of the shell growth, by a continuum transfer of material on top of the energetically unfavorable {11-20} facets, which is enriched in Ge due to its higher mobility compared to Si.

These Ge-rich prisms will have a smaller band gap compared to the remaining of the shell which is unwanted when aiming for a uniform SiGe shell. The prism can however be exploited on purpose, as behaving like additional and smaller NWs running within the core-shell NW, e.g. for confinement effects. The possibility of tuning the prism geometry by controlling the GaP-Si morphology, e.g. by setting the GaP overgrowth on the VLS core, is an additional design parameter in that respect.

It is finally worth noting that, despite the massive material transfers revealed by the prisms segregation, the SiGe shell preserves its hexagonal phase, even if metastable, proving the robustness of the growth method.

Author contributions

R.B., R.P., F.M., E.B. and L.M. designed the research. R.B. and M.A. developed the phase-field model and performed the simulations. E.S. performed the ab-initio calculations. Y.R. and I.H. performed the growth experiments. S.K. and M.V. performed the structural and compositional analysis. R.B., R.P. and M.A. wrote the manuscript. All authors discussed the results and revised the manuscript.

Conflicts of interest

There are no conflicts to declare.

Acknowledgement

Solliance and the Dutch Province of Noord-Brabant are acknowledged for funding the TEM facility. This work is supported by NanoNextNL, a micro and nanotechnology consortium of the Government of the Netherlands and 130 partners. We acknowledge the CINECA award under the ISCRA initiative, for the availability of high-performance computing resources and support.

References

1 C. Jia, Z. Lin, Y. Huang and X. Duan, *Chem. Rev.*, 2019, **119**, 9074–9135.
2 L. Güniat, P. Caroff and A. Fontcuberta i Morral, *Chem. Rev.*, 2019, **119**, 8958–8971.
3 M. Heiss, Y. Fontana, A. Gustafsson, G. Wüst, C. Magen, D. D. O’Regan, J. W. Luo, B. Ketterer, S. Conesa-Boj, a V Kuhlmann, J. Houel, E. Russo-Averchi, J. R. Morante, M. Cantoni, N. Marzari, J. Arbiol, A. Zunger, R. J. Warburton and A. Fontcuberta i Morral, *Nat. Mater.*, 2013, **12**, 439–444.
4 T. Shi, H. E. Jackson, L. M. Smith, N. Jiang, Q. Gao, H. H. Tan, C. Jagadish, C. Zheng and J. Etheridge, *Nano Lett.*, 2015, **15**, 1876–1882.
5 N. I. Goktas, P. Wilson, A. Ghukasyan, D. Wagner, S.

McNamee and R. R. LaPierre, *Appl. Phys. Rev.*, 2018, **5**, 041305.
6 S. W. Eaton, A. Fu, A. B. Wong, C.-Z. Ning and P. Yang, *Nat. Rev. Mater.*, 2016, **1**, 16028.
7 R. M. Lutchyn, E. P. A. M. Bakkers, L. P. Kouwenhoven, P. Krogstrup, C. M. Marcus and Y. Oreg, *Nat. Rev. Mater.*, 2018, **3**, 52–68.
8 M. Albani, S. Assali, M. A. Verheijen, S. Koelling, R. Bergamaschini, F. Pezzoli, E. P. A. M. Bakkers and L. Miglio, *Nanoscale*, 2018, **10**, 7250–7256.
9 H. I. T. Hauge, M. A. Verheijen, S. Conesa-Boj, T. Etzelstorfer, M. Watzinger, D. Kriegner, I. Zardo, C. Fasolato, F. Capitani, P. Postorino, S. Kölling, A. Li, S. Assali, J. Stangl and E. P. A. M. Bakkers, *Nano Lett.*, 2015, **15**, 5855–5860.
10 E. M. T. Fadaly, A. Dijkstra, J. R. Suckert, D. Ziss, M. A. J. van Tilburg, C. Mao, Y. Ren, V. T. van Lange, K. Korzun, S. Kölling, M. A. Verheijen, D. Busse, C. Rödl, J. Furthmüller, F. Bechstedt, J. Stangl, J. J. Finley, S. Botti, J. E. M. Haverkort and E. P. A. M. Bakkers, *Nature*, 2020, **580**, 205–209.
11 N. Sköld, J. B. Wagner, G. Karlsson, T. Hernán, W. Seifert, M.-E. Pistol and L. Samuelson, *Nano Lett.*, 2006, **6**, 2743–2747.
12 J. B. Wagner, N. Sköld, L. Reine Wallenberg and L. Samuelson, *J. Cryst. Growth*, 2010, **312**, 1755–1760.
13 D. Rudolph, S. Funk, M. Döblinger, S. Morkötter, S. Hertenberger, L. Schweickert, J. Becker, S. Matich, M. Bichler, D. Spirkoska, I. Zardo, J. J. Finley, G. Abstreiter and G. Koblmüller, *Nano Lett.*, 2013, **13**, 1522–1527.
14 X. Yuan, P. Caroff, J. Wong-Leung, H. H. Tan and C. Jagadish, *Nanoscale*, 2015, **7**, 4995–5003.
15 L. Balaghi, G. Bussone, R. Grifone, R. Hübner, J. Grenzer, M. Ghorbani-Asl, A. V. Krasheninnikov, H. Schneider, M. Helm and E. Dimakis, *Nat. Commun.*, 2019, **10**, 2793.
16 C. Zheng, J. Wong-Leung, Q. Gao, H. H. Tan, C. Jagadish and J. Etheridge, *Nano Lett.*, 2013, **13**, 3742–3748.
17 Y. Zhang, A. M. Sanchez, J. Wu, M. Aagesen, J. V. Holm, R. Beanland, T. Ward and H. Liu, *Nano Lett.*, 2015, **15**, 3128–3133.
18 A. C. Meng, M. R. Braun, Y. Wang, C. S. Fenrich, M. Xue, D. R. Diercks, B. P. Gorman, M. I. Richard, A. F. Marshall, W. Cai, J. S. Harris and P. C. McIntyre, *Mater. Today Nano*, 2019, **5**, 100026.
19 R. Bergamaschini, F. Montalenti and L. Miglio, *Appl. Surf. Sci.*, 2020, **517**, 146056.
20 H. A. Fonseka, Y. Zhang, J. A. Gott, R. Beanland, H. Liu and A. M. Sanchez, *Nano Res.*, 2021, **12**, 157–164.
21 L. Francaviglia, G. Tütüncüoglu, S. Martí-Sánchez, E. Di Russo, S. Escobar Steinvall, J. Segura Ruiz, H. Potts, M. Friedl, L. Rigutti, J. Arbiol and A. Fontcuberta i Morral, *Phys. Rev. Mater.*, 2019, **3**, 023001.
22 B. Zhang, M. Jansson, Y. Shimizu, W. M. Chen, F. Ishikawa and I. A. Buyanova, *Nanoscale*, 2020, **12**, 20849–20858.
23 G. Schmidt, M. Müller, P. Veit, S. Metzner, F. Bertram, J. Hartmann, H. Zhou, H.-H. Wehmann, A. Waag and J. Christen, *Sci. Rep.*, 2018, **8**, 16026.
24 J. Arbiol, C. Magen, P. Becker, G. Jacopin, A. Chernikov, S. Schäfer, F. Furtmayr, M. Tchernycheva, L. Rigutti, J. Teubert, S. Chatterjee, J. R. Morante and M. Eickhoff, *Nanoscale*, 2012, **4**, 7517–7524.
25 S. Assali, R. Bergamaschini, E. Scalise, M. A. Verheijen, M. Albani, A. Dijkstra, A. Li, S. Koelling, E. P. A. M. Bakkers, F. Montalenti and L. Miglio, *ACS Nano*, 2020, **14**, 2445–2455.
26 H. A. Fonseka, A. V. Velichko, Y. Zhang, J. A. Gott, G. D. Davis, R. Beanland, H. Liu, D. J. Mowbray and A. M. Sanchez, *Nano Lett.*, 2019, **19**, 4158–4165.
27 M. H. T. Dastjerdi, E. M. Fiordaliso, E. D. Leshchenko, A. Akhtari-Zavareh, T. Kasama, M. Aagesen, V. G. Dubrovskii and R. R. LaPierre, *Nano Lett.*, 2017, **17**, 5875–5882.
28 S. Funk, M. Royo, I. Zardo, D. Rudolph, S. Morkötter, B. Mayer, J. Becker, A. Bechtold, S. Matich, M. Döblinger, M. Bichler, G. Koblmüller, J. J. Finley, A. Bertoni, G. Goldoni and G. Abstreiter, *Nano Lett.*, 2013, **13**, 6189–6196.
29 H. I. T. Hauge, S. Conesa-Boj, M. A. Verheijen, S. Koelling and E. P. A. M. Bakkers, *Nano Lett.*, 2017, **17**, 85–90.
30 Y. Ren, P. Leubner, M. A. Verheijen, J. E. M. Haverkort and E. P. A. M. Bakkers, *Nanotechnology*, 2019, **30**, 295602.
31 S. Conesa-Boj, H. I. T. Hauge, M. A. Verheijen, S. Assali, A. Li, E. P. A. M. Bakkers and A. Fontcuberta i Morral, *Nano Lett.*, 2015, **15**, 2974–2979.
32 C. Raffy, J. Furthmüller and F. Bechstedt, *Phys. Rev. B*, 2002, **66**, 075201.
33 C. Rödl, J. Furthmüller, J. R. Suckert, V. Armuzza, F. Bechstedt and S. Botti, *Phys. Rev. Mater.*, 2019, **3**, 1–11.
34 L. Canham, *Nature*, 2000, **408**, 411–412.
35 G. Biasiol and E. Kapon, *Phys. Rev. Lett.*, 1998, **81**, 2962–2965.
36 S. Assali, I. Zardo, S. Plissard, D. Kriegner, M. A. Verheijen, G. Bauer, A. Meijerink, A. Belabbes, F. Bechstedt, J. E. M. Haverkort and E. P. A. M. Bakkers, *Nano Lett.*, 2013, **13**, 1559–1563.
37 E. J. Kirkland, R. F. Loane and J. Silcox, *Ultramicroscopy*, 1987, **23**, 77–96.
38 R. Backofen, R. Bergamaschini, A. Voigt, F. Montalenti and A. Voigt, *Philos. Mag.*, 2014, **94**, 2162–2169.
39 B. Li, J. Lowengrub, A. Rätz and A. Voigt, *Commun. Comput. Phys.*, 2009, **6**, 433–482.
40 L. Huang, F. Liu, G.-H. H. Lu and X. G. Gong, *Phys. Rev. Lett.*, 2006, **96**, 016103–016106.
41 R. Bergamaschini, J. Tersoff, Y. Tu, J. J. Zhang, G. Bauer and F. Montalenti, *Phys. Rev. Lett.*, 2012, **109**, 156101.
42 B. Li, J. Lowengrub, A. R and A. Voigt, *Physics (College. Park. Md).*, 2009, **6**, 433–482.
43 J. Tersoff, *Appl. Phys. Lett.*, 2003, **83**, 353–355.
44 B. J. Spencer, *Phys. Rev. E*, 2004, **69**, 011603.
45 M. Salvalaglio, R. Backofen, R. Bergamaschini, F. Montalenti and A. Voigt, *Cryst. Growth Des.*, 2015, **15**, 2787–2794.
46 E. Scalise, A. Sarikov, L. Barbisan, A. Marzegalli, D. B. Migas, F. Montalenti and L. Miglio, *Appl. Surf. Sci.*, 2021, 148948.
47 S. Vey and A. Voigt, *Comput. Vis. Sci.*, 2007, **10**, 57–67.
48 T. Witkowski, S. Ling, S. Praetorius and A. Voigt, *Adv. Comput. Math.*, 2015, **41**, 1145–1177.
49 S. Koelling, R. C. Plantenga, H. I. T. Hauge, Y. Ren, A. Li, M. A. Verheijen, S. Conesa Boj, S. Assali, P. M. Koenraad and E. P. A. M. Bakkers, *ECS Trans.*, 2016, **75**, 751–760.

View Article Online
DOI: 10.1039/D0NR08051A

50 R. Nötzel, L. Däweritz and K. Ploog, *Phys. Rev. B*, 1992, **46**, 4736–4743.